DOI 10.4430/bgo00390

Topography incorporated inversion of DC resistivity data using integral equation vs. Res2dinv software

R. Varfinezhad[1], H. Ghari[2] and R. Rafiei[1]

[1] *Institute of Geophysics, University of Tehran, Iran*
[2] *Department of Mining and Metallurgical Engineering, Yazd University, Yazd, Iran*

(Received: 26 October 2021; accepted: 1 April 2022; published online: 23 June 2022)

ABSTRACT In this paper, the direct-current (DC) resistivity inversion problem, based on the integral equation (IE), is expanded to data sets, including uneven topography, which has never been done before. For the inversion procedure, a weighted damped minimum length solution is implemented and depth weighting is used as the model weighting matrix. The regularisation parameter is estimated utilising an initial guess equal to the maximum value of the kernel matrix (forward operator). Then, the optimal value is adopted by a few trials and errors. To investigate the productivity of the presented method, the inversion results are compared with the inversion models derived from Res2dinv software, which works based on nonlinear equations. At first, a model of a conductive dyke under a valley is considered for which the retrieved model by the extended IE technique is even superior to the Res2dinv result. Because of the promising consequence derived from the synthetic case, the efficiency of the presented method is tested on the data set of the Robat Sang mine in Iran. The inversion model obtained from the extended IE method shows a high consistency with Res2dinv.

Key words: DC resistivity, uneven topography, integral equation, inversion, Res2dinv.

1. Introduction

The direct current (DC) resistivity is a well-established, non-destructive, cost-effective, and powerful subsurface imaging approach to understanding the Earth's subsurface structures. The DC resistivity method is widely used for mineral resource explorations (Shin *et al.*, 2021), hydrogeophysical investigations (Szűcs *et al.*, 2021), environmental and engineering purposes (Demirci *et al.*, 2012), detecting archaeological targets (Tsokas *et al.*, 2008), and vulcanology (Fikos *et al.*, 2012).

DC resistivity applications are industrially feasible if a reasonably fast algorithm is accurate enough to invert the survey data. In these applications, DC resistivity data are generally acquired along with several profiles and interpreted using 2D or 3D inversion algorithms. These algorithms have been developed with plenty of methods based on finite elements [FE: Sasaki (1994)], finite differences [FD: Spitzer (1995)], and integral equations [IE: Perez-Flores *et al.* (2001)].

There are many DC resistivity surveys that are carried out in mountainous regions; hence, they are deeply influenced by local variations in surface resistivity caused by rugged topography, i.e. generated by weathering and moisture content (Fox *et al.*, 1980; Telford *et al.*, 1990). Many researches have been conducted in this field (Fox *et al.*, 1980; Tong and Yang, 1990; Loke, 2000; Rücker *et al.*, 2006; Lu *et al.*, 2015). Researchers have found that at the surface of the

homogeneous ground, the current distribution is concentrated in a valley and diverged beneath hills, and subsequently, the equipotential surfaces are distorted (Fox *et al.*, 1980). The type of the array and the position of the survey lines can complicate the topographic effects (Tsourlos *et al.*, 1995).

High-resistivity structures appear below the central hills and ridges, whereas the transitions from the hill and ridge to the planes on the left- and right-hand sides show low resistivity anomalies. A valley produces just the opposite anomaly pattern: a central low flanked by highs. A slope generates low resistivity values at its base and high values at its top as a result (Fox *et al.*, 1980; Telford *et al.*, 1990; Lu *et al.*, 2015). Besides, with the increase of slope angle, topographic resistivity anomalies become more marked (Fox *et al.*, 1980; Lu *et al.*, 2015).

The DC resistivity measurements are also sensitive to the direction where the electrodes lines are laid; topography, when the electrode line is parallel, rather than normal, to its strike, could also moderately affect the results (Telford *et al.*, 1990; Lu *et al.*, 2015). Tsourlos *et al.* (1995) show that four-electrode arrays are less sensitive to terrain topography variations than arrays using remote probes. A Wenner array straddling an irregular ground surface produces resistivity reflections (Tsourlos *et al.*, 1995; Lu *et al.*, 2015), just the opposite to the results of dipole-dipole (Coggon, 1971; Fox *et al.*, 1980; Shi-zhe, 1993; Tsourlos *et al.*, 1995) and pole-pole arrays (Tsourlos *et al.*, 1995; Lu *et al.*, 2015) described above. Tsourlos *et al.* (1995) compare the effects of topography on the performance of various resistivity arrays.

Topographic effects in DC resistivity surveys described above are fundamentally caused by flat-Earth geometric factors to compute apparent resistivity over an irregular terrain (Fox *et al.*, 1980; Telford *et al.*, 1990). These effects make anomalies mislead and generate inaccurate interpretations of the data (Fox *et al.*, 1980; Telford *et al.*, 1990; Tsourlos *et al.*, 1999), especially in areas where resistivity contrasts between geologic units are not high, and slope angles are more than 10° (Fox *et al.*, 1980; Tsourlos *et al.*, 1995) or 15° (Lu *et al.*, 2015). Therefore, predicting surface topography effects and taking them into account in the interpretation techniques have been studied by many researchers (Sasaki, 1994). There are two methods to remove the topography effect: 1) modelling-incorporating topography and 2) inversion-incorporating topography.

In the first method, correction procedures have been suggested before using an inversion technique to remove or reduce topographic effects. Fox *et al.* (1980) have formulated a terrain correction procedure using a 2D FE modelling program to minimise the effect of the topography in DC resistivity surveys using the dipole-dipole array. This approach was extended to 3D by Holcombe and Jiracek (1984) by implementing a 3D FE code. Moreover, Oppliger (1984) and Tsourlos *et al.* (1995) have introduced topographic correction in which the apparent resistivity value for a homogeneous model with the true topography is calculated using the FE method and the results are used to correct the measured data. Penz *et al.* (2013) propose a secondary potential technique employing the generalised finite difference method. Shi-zhe (1993) uses the boundary element (BE) method to solve the problem of the effect of 2D terrain with point current source on DC resistivity surveys. In theory, these topographic correction approaches are precise if the subsurface models are homogeneous. Consequently, in complicated media, the resistivity response may not be separated entirely from the effect of the topography when using the topographic corrections through the modelling (Tong and Yang, 1990).

A practical solution to overcome the above problem is to include a forward solution scheme capable of modelling topography into inversion algorithms. However, few studies have focused on the systematic research of topography effects based on modelling and inversion. Examples of these DC resistivity inversions, including topography, can be found in Tong and Yang (1990),

Sasaki (1994), Loke (2000), Pain *et al.* (2002), Günther *et al.* (2006), Demirci *et al.* (2012) and Lu *et al.* (2015).

This paper extends DC resistivity inversion modelling based on the IE method for data, including uneven topography, which has not previously been undertaken. Firstly, the forward operator is defined for the data sets with uneven topography. Then, the inversion method is introduced, the weighted damped minimum length solution, and depth weighting is used as the model weighting function. The usefulness of the presented technique is investigated by synthetic and real data sets and the results are also compared with Res2dinve inversion models.

2. Methodology

This section briefly explains forward modelling for flat topography introduced by Perez-Flores (1995). It is then broadened to uneven topography and finally the inversion algorithm is presented.

2.1. Forward modelling for flat topography

For DC resistivity measurements taken with four electrode arrays, Perez-Flores (1995) utilised the Born approximation and related apparent resistivity ρ_a to the true resistivity ρ through the following linear IE:

$$\log\rho_a(x_A, x_B, x_M, x_N) = \frac{[g]^{-1}}{\pi}\int_0^{\infty}\int_{-\infty}^{\infty} K(x_A, x_B, x_M, x_N)\log\rho\,(x,z)dxdz \tag{1}$$

x_A, x_B, x_M, and x_N stand for the coordinates of electrodes *A*, *B*, *M*, and *N*, respectively, *g* is the geometrical factor and the kernel function *K* is defined as:

$$K(x_A, x_B, x_M, x_N) = N(x_A, x_M) - N(x_B, x_M) - N(x_A, x_N) + N(x_B, x_N) \tag{2}$$

where (Charré-Meza *et al.*, 2000):

$$N(x_i, x_j) = \int_{-\infty}^{\infty} \frac{(x - x_i)(x_j - x) - y^2 - z^2}{\sqrt{((x - x_i)^2 + y^2 + z^2)^3\,((x_j - x)^2 + y^2 + z^2)^3}}dy\,, \qquad \begin{cases} i = A, B \\ j = M, N \end{cases}. \tag{3}$$

For the 2D problem, *P* measured data points are considered and the subsurface in question is discretised into *Q* prismatic cells with constant resistivity, which are elongated infinitely in the *y*-direction (Fig. 1a). So, we may form the system:

$$\mathbf{d} = \mathbf{Am} \tag{4}$$

d is a column vector of P log (ρ_a) data and the vector **m** includes the Q log ρ unknowns. Therefore, **A** is a $P \times Q$ matrix with elements computed using the following equation:

$$A_{ij} = \int_{\Delta x_j} \int_{\Delta z_j} \left[2 \int_0^{\infty} K_i(x', y', z') dy' \right] dx' dz' \tag{5}$$

x' and z' are coordinates of cell centres. To obtain forward operator matrix **A**, Eq. 5 should be solved for which the following steps are required:

i) $\int_0^{\infty} K_i(x', y', z') dy'$ must be solved to obtain a 2D case and this can be done using numerical integration by implementing the midpoint rule;

ii) since the subsurface is discretised into Q prismatic cells, we should compute the effect of cell j at the observation point i as A_{ij} element of matrix **A**. If we do this for all cells and observation points, matrix **A** is computed.

Eq. 5 is a Fredholm IE of the first kind and readers are referred to Aster *et al.* (2018) to understand the discretisation procedure of a Fredholm IE of the first kind as well as the midpoint rule.

2.2. Incorporating uneven topography in the forward operator

Setting z_{min} and z_{max} as the minimum and maximum elevations of the interested area, respectively, the source volume will be in the interval [z_{min}, z_{max} + dz] along the z axis, where dz is the cell thickness (Fig. 1b).

The curve defined by the electrode positions is approximated by a stepped line, as we fixed their x and z coordinates. Since the forward operator **A** depends on the coordinates of data points, uneven topography may play an important role in the inversion process. For a satisfactory approximation to the topography curve, we suggest using cells long one-fourth of the minimum electrode spacing. On the one hand, incorporating more cells will allow a better approximation to the topography; on the other hand, this means more unknowns for the inverse procedure. For an ill-posed problem, increasing the number of cells can also worsen its ill-posedness. Therefore, we should find a trade-off to define the number of cells.

Incorporating uneven topography in the forward operator leads to modify Eq. 3 as:

$$N(x_i, x_j, z_i, z_j, x', z') = \int_{-\infty}^{\infty} \frac{(x' - x_i)(x_j - x') - y'^2 - (z' - z_i)(z_j - z')}{\sqrt{((x' - x_i)^2 + y'^2 + (z' - z_i)^2)^3 \left(\left(x_j - x'\right)^2 + y'^2 + \left(z_j - z'\right)^2\right)^3}} dy' \quad \begin{cases} i = A, B \\ j = M, N \end{cases} \tag{6}$$

where x' and z' are coordinates of cell centres and z_i and z_j are the vertical coordinates of current and potential electrodes, respectively.

For topography included data sets, i) the z coordinates of the electrodes should be inserted and ii) the distance between electrodes using their x and z coordinates computed. This issue is very important because, for instance, we should know the distance between electrodes A and B and B and M to obtain n = BM/AB for dipole-dipole array. This computed value can be non-

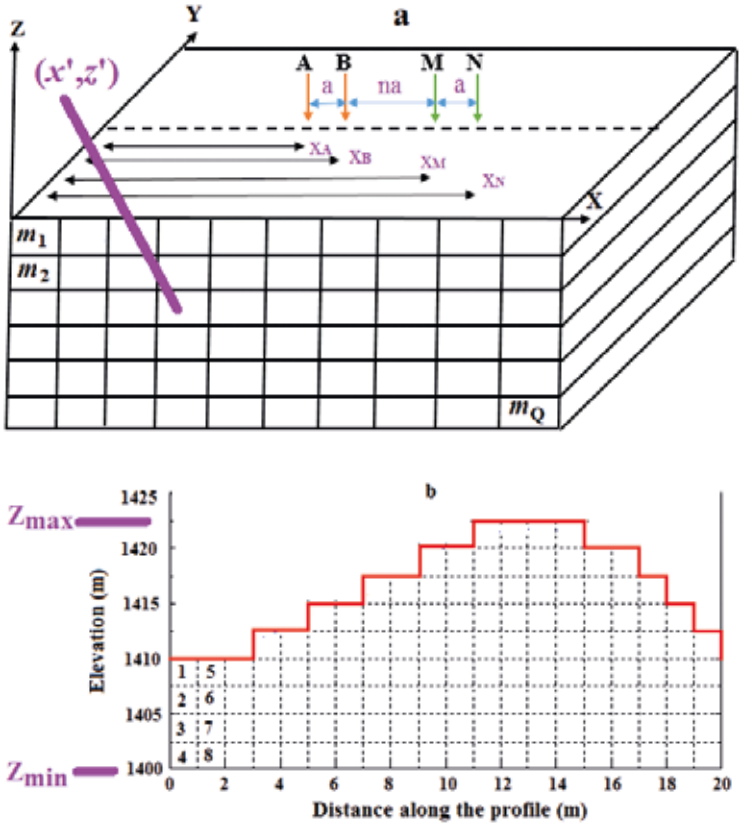

Fig. 1 - (a) Discretisation of the source volume into a set of homogeneously resistive prisms. The dipole-dipole array is on the measurement area; *x'* and *z'* refer to the prism centres (Varfinezhad *et al.*, 2020), n can be any real value larger than 1, but it is usually an integer. (b) Discretising the survey area in question into a surface containing equal size cells. We show a vertical section where the red curve represents the approximated topography of the survey region. During the inversion procedure, only cells under the topography curve are considered.

integer and different from what is in question before data collection for the surveys with uneven topography.

2.3. Inversion method

Eq. 4 is a linear problem and, to find a realistic solution, the following objective function must be minimised (Tikhonov and Arsenin, 1977):

$$\|\mathbf{W_d}(\mathbf{Am}-\mathbf{d})\|_2^2+\mu\|\mathbf{W_m}(\mathbf{m}-\mathbf{m_0})\|_2^2 \tag{7}$$

$\mathbf{m_0}$ is the initial model and will be updated during the iterative inversion algorithm. $\mathbf{W_d}$, $\mathbf{W_m}$ and μ are data weighting matrix, model weighting matrix, and regularisation parameter, respectively. For simplicity, we will here assume independent measurements with unit variance so that $\mathbf{W_d} = \boldsymbol{I}$. The final inversion model can be obtained using a weighted damped minimum length solution (Menke, 2012):

$$\mathbf{m}_k=\mathbf{m}_{k-1}+(\mathbf{W}_m^{-1}\mathbf{A}^{\mathrm{T}})(\mathbf{A}\mathbf{W}_m^{-1}\mathbf{A}^{\mathrm{T}}+\mu\mathbf{I})^{-1}(\mathbf{d}-\mathbf{A}\mathbf{m}_{k-1}) \tag{8}$$

$\mathbf{W}_m$ has been often chosen as $\mathbf{W}_m = \mathbf{C}^{\mathrm{T}}\mathbf{C}$ for DC resistivity inversion where $\mathbf{C}$ can be the steepness matrix or even the roughness matrix. In this paper, we use a depth weighting matrix for $\mathbf{W}_m$ as:

$$\mathbf{W}_m = \frac{1}{\mathbf{z}_c{}^{\beta/2}} \tag{9}$$

where $\boldsymbol{z}_c$ is the depth coordinate vector of the cell centres and β is the depth weighting exponent.

The depth weighting (Eq. 10) has frequently been used in magnetic and gravity data inversions (e.g. Li and Oldenburg, 1996, 1998; Boulanger and Chouteau, 2001; Cella and Fedi, 2012; Paoletti *et al.*, 2013; Varfinezhad *et al.*, 2019; Varfinezhad and Ardestani, 2022), but was introduced for inversion of DC resistivity data and its joint inversion by Varfinezhad *et al.* (2020).

Regularisation parameter and depth weighting exponent are the critical parameters in the inversion procedure. Regularisation parameter can be estimated using L-curve or generalised cross validation (GCV) techniques, but a different approach is used here. First, we have an initial guess equal to the maximum value of the forward operator (MaxKer), then the optimal value is adopted from the interval (0.1 × MaxKer - 3 × MaxKer) by a few trials and errors. For most cases, this optimal value is equal or close to MaxKer and Appendix A shows why this is true. Varfinezhad and Ardestani (2022) showed that MaxKer might be used for the regularisation parameter estimation in the inversion of gravity data. Inversion of noisy data usually requires values larger than MaxKer. The considered synthetic real data cases support this experimental estimation of the regularisation parameter.

However, depth weighting is utilised for DC resistivity inversion but there is no specific and comprehensive study about its role in DC resistivity data inversion and how depth weighting exponent should be determined. Synthetic modelling shows that, for compact bodies, 2 can be the best adoption for the exponent of depth weighting function.

2.4. Synthetic modelling for investigation of depth weighting exponent

The synthetic model comprises four conductive sources with 20 Ω·m resistivity surrounded by a homogenous background with 100 Ω·m resistivity (see Fig. 2). A dipole-dipole array with 10 m dipole separation is used to calculate synthetic data; apparent resistivities are computed for *n* from 1 to 9. We will examine the effect of depth weighting exponent on the IE inversion algorithm.

The inversion results of the observed synthetic data using a dipole-dipole array for different exponent values (from 0 to 4), alongside the inversion model derived from Res2dinv software, are displayed in Fig. 3. Regularisation parameter and number of iterations are fixed as μ = 0.2 and k_{max} = 10, respectively.

The most notable features arising from the different inversions are:

I) similar to gravity and magnetic inversion, high b leads to the model deep sources;

II) some instability is observed for high β;

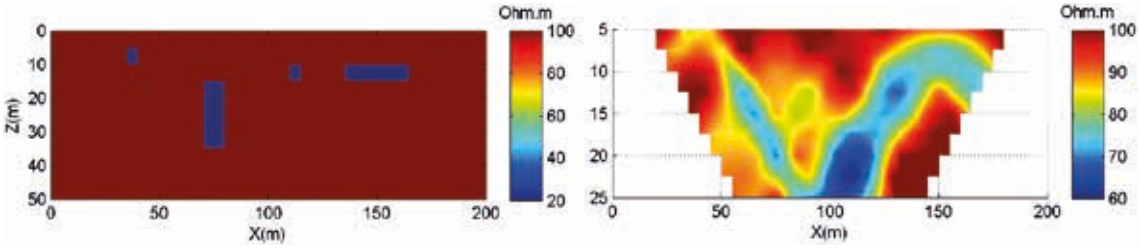

Fig. 2 - Four conductive anomalies of 20 Ω·m surrounded by a resistive homogenous medium of 100 Ω·m (left) and its forward apparent resistivity pseudo section response calculated by Res2dmod software (right).

III) low β leads to too resistive sources; the tabular source seems better characterised by low $\beta = 1$; $\beta = 2$ seems to be the best choice for the whole set of sources; $\beta = 4$ leads to image some false sources;
IV) the regularisation used in the Res2dinv software leads tendentially to deeply elongated sources. The rightmost source, having a tabular shape, is the less well represented.

In our case, however, it seems that $\beta = 2$ could be a good compromise, for block-type sources of tabular, compact or vertically elongated shape.

The trend of root mean square (RMS) misfit error values for $\beta = 2$ is represented in Fig. 5a, which shows 10 iterations are enough for stopping the inversion algorithm.

The inversion models obtained for other arrays are reported in Appendix A (Fig. A1).

3. Synthetic modelling for uneven topography

To investigate the performance of the extended IE method with uneven topography, we here describe the case of a thin conductive dyke (25 Ω·m) under a valley with a resistive background of 100 Ω·m. Model and resistivity pseudosection of true data are shown in Figs. 4a and 4d, respectively. The number of data is 61 with unit dipole separation (*a* in Fig. 1a) and *n* from 1 to 6. Number of electrodes is 17. Regularisation parameter and depth weighting exponent for the extended IE inversion are obtained using the described criterion. Since the MaxKer is 0.78, it is used as the initial guess for the estimation regularisation parameter. During 3 trial and errors, we may find 0.1 × MaxKer = 0.078 is the optimal choice for the regularisation parameter. According to the test done in the previous section, the depth weighting exponent adopted to be 2 and the iterative inversion procedure is stopped after 25 iterations when there is no significant decrease in RMS error values (Table 1). The RMS misfit error values calculated from the IEDW solution for each iteration are shown in Fig. 5b.

Table 1 - RMS error values in the last 8 iterations.

Iteration Number	18	19	20	21	22	23	24	25
RMS error (%)	2.71	2.67	2.63	2.59	2.55	2.52	2.49	2.46

Inversion models obtained from the IE and Res2dinv software are shown in Figs. 4b and 4c. The resistivity model in Fig. 4b confirms the good performance of the IE inversion algorithm, which allows a reasonable reconstruction of the thin conductive dyke. The misfit of recovered models by IE and Res2dinv relative to the true model are displayed in Figs. 4e and 4f, demonstrating better performance by the expanded IE inversion algorithm. Res2dinv algorithm reconstructs the dyke with a larger lateral thickness. Both kinds of models show artifacts, especially the Res2dinv one. RMS misfit of the computed data for IE and Res2dinv are 2.46 and 1.4%, respectively.

4. Real data

Finally, we evaluate the performance of the IE inversion algorithm for DC resistivity data in a mining district (Iran), characterised by uneven topography. This data set is collected using a dipole-dipole array on the Robat Sang mine, near Mashhad in Iran (Fig. 6). Separation of the

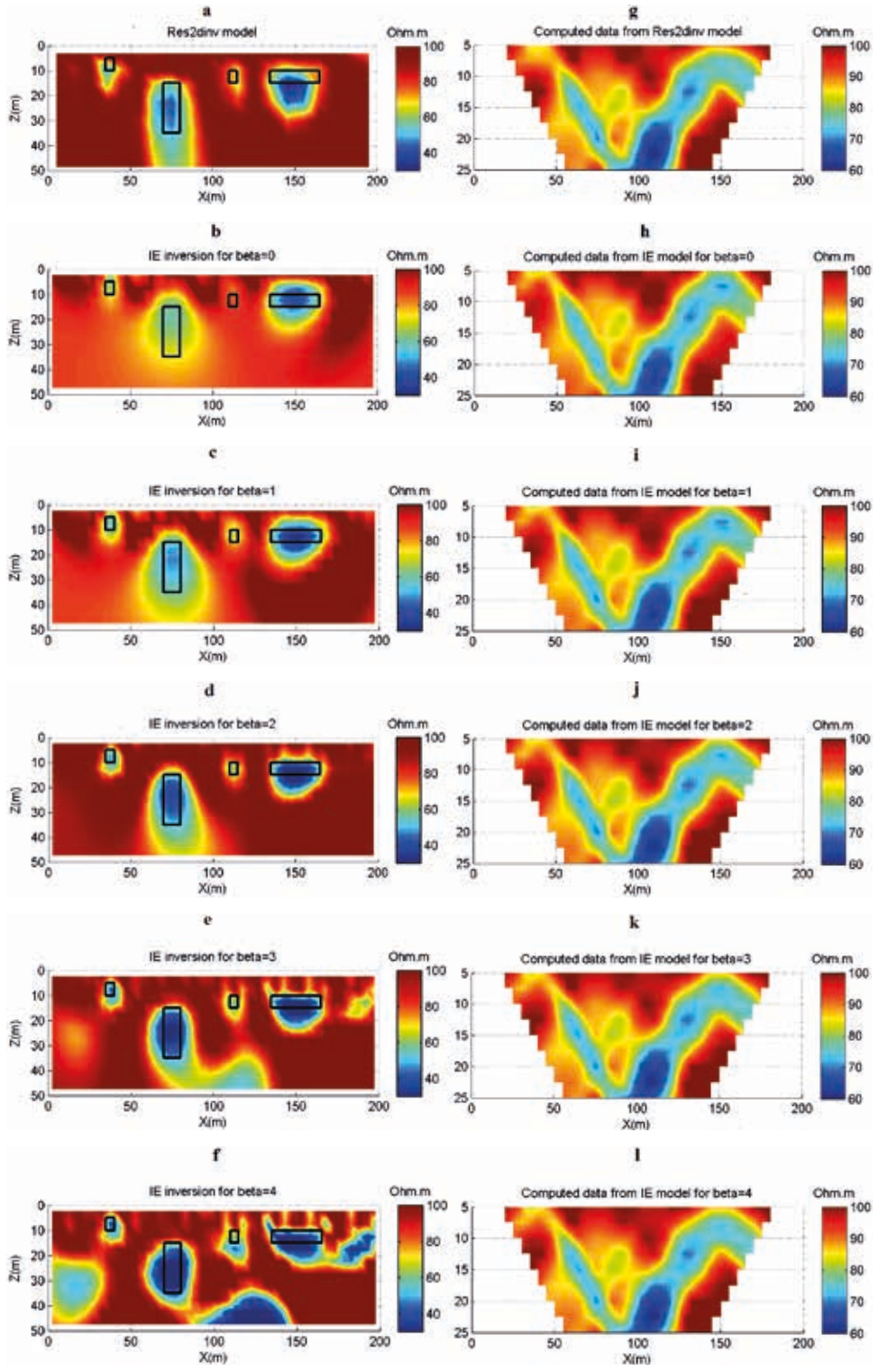

Fig. 3 - Inversion models derived from Res2dinv algorithm (a), IE depth weighted (IEDW) with $\beta = 0$ (b), IEDW with $\beta = 1$ (c), IEDW with $\beta = 2$ (d), IEDW with $\beta = 3$ (e), IEDW with $\beta = 4$ (f). Pseudo-section of observed data (g), computed data with $\beta = 0$ (h), computed data with $\beta = 1$ (i), computed data with $\beta = 2$ (j), computed data with $\beta = 3$ (k), computed data with $\beta = 4$ (l).

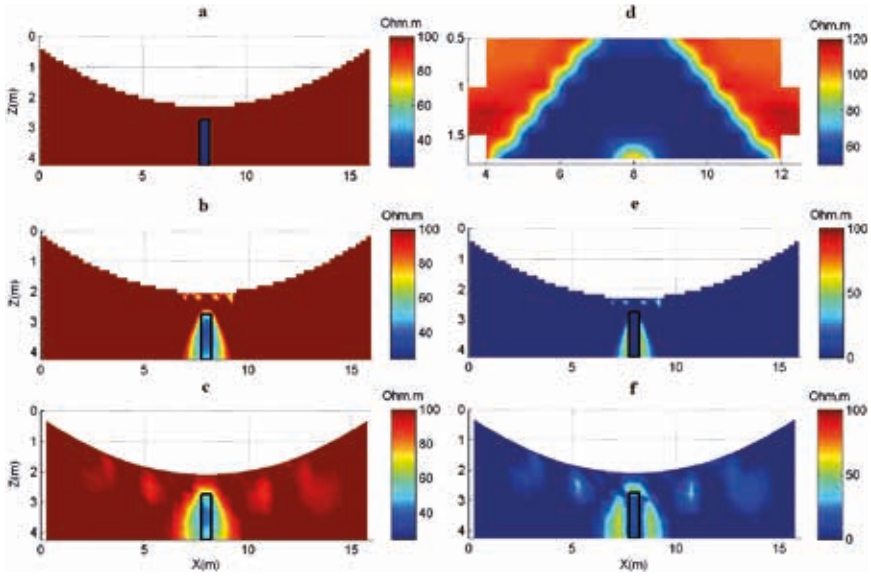

Fig. 4 - A thin conductive dyke model with uneven topography (a). The inverted model derived from the IEDW inversion algorithm (b) and Res2dinv software (c). Pseudo-sections of apparent resistivities obtained from the measurements (d). Misfit inversion sections of IEDW inversion model (e) and Res2dinv inversion model (f), respectively.

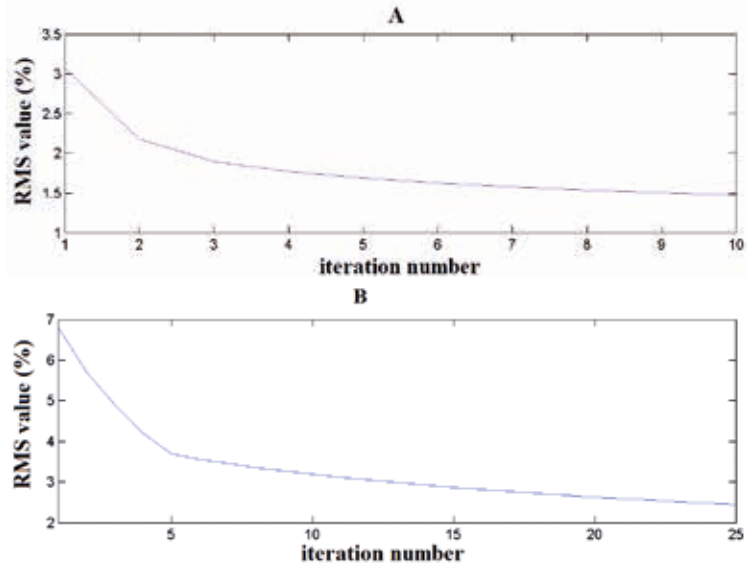

Fig. 5 - Curves of data misfit RMS errors for: a) multisource case with b = 2 and b) dyke model.

Afghan block from the bedrock during Cenomanian has caused the deposition of the oceanic mantle and oceanic crust-associated ophiolitic bedrock in the area; this ophiolite rock unit is at the base of chromite and copper mineralisation potential in the area. The collision of the Arabian Plateau on the central Iranian block has caused orogenic activity from N-NW to S-SW of most of Iran; due to the clockwise rotations of the Lut and Hilmand blocks, this structural pattern represents a very complex structure and is indicative of an intercontinental orogeny in these areas. This rotation is the main cause of severe tectonics and different alteration zones in the region. Due to active tectonics in this area, the faults act as channels and cause mineralisation of copper carbonates (malachite).

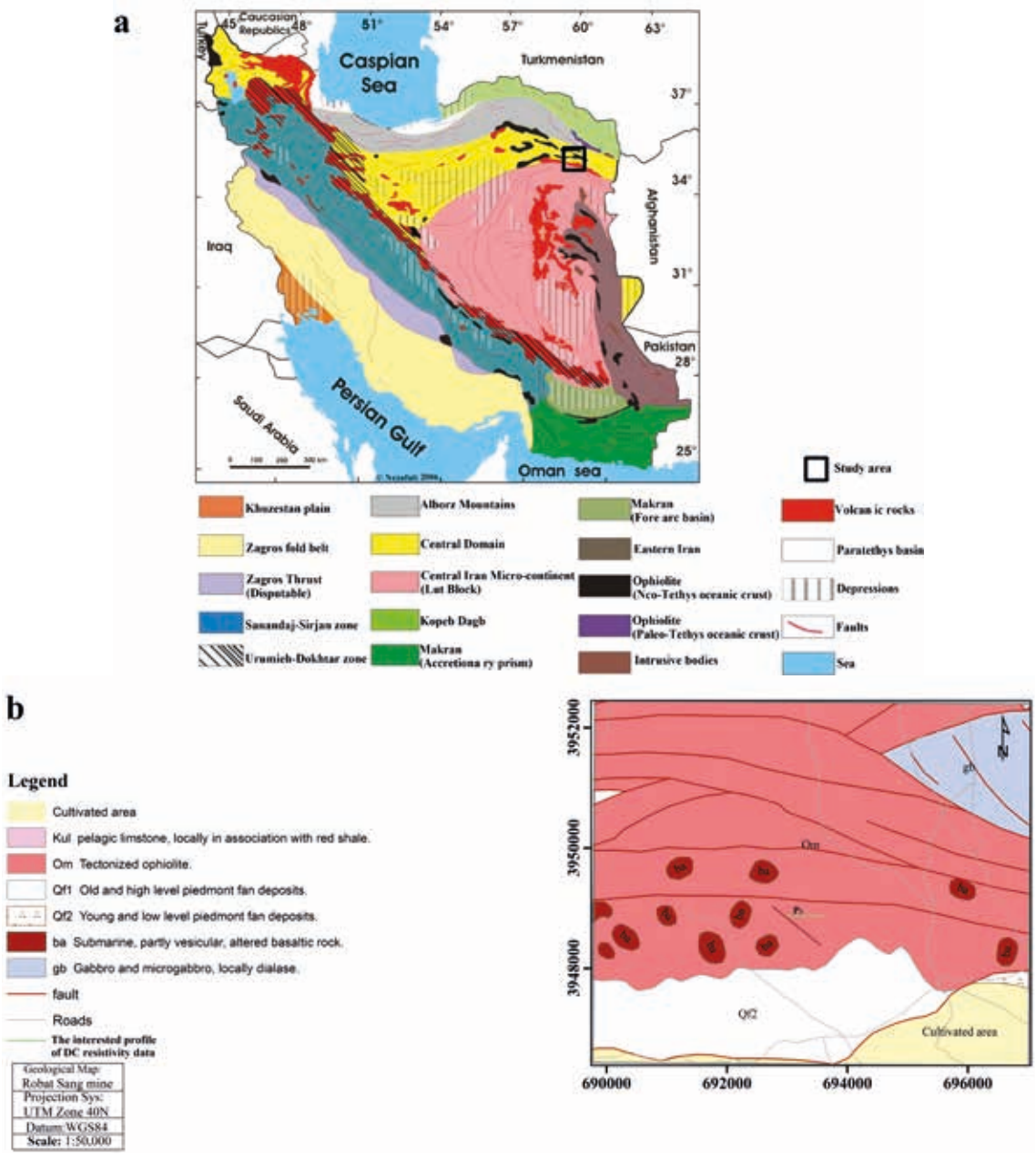

Fig. 6 - Geographic map of Iran (a), the relevant area is marked with a purple rectangle (Barahoei *et al.*, 2014) and geological map of the Robat Sang mine area (b), near Mashhad in Iran (Geological Survey of Iran).

Dipole separation and number of data are 15 m and 128, respectively. Reconstructed models from this data set derived by IE and Res2dinv inversions are shown in Figs. 7a and 7b. Both of them show three main sources, marked with numbers 1, 2, and 3 on the inversion sections. In addition, the IP inverse section retrieved by Res2dinv is shown in Fig. 7c. For the IE inversion algorithm, anomaly 1 is next to the surface and its horizontal extension lies in the interval of [100 m, 1500 m] with vertical extension from the surface to the elevation about 1665 m; anomaly 2 ranges from 160 to 200 m and extends from 1640 to 1660 m elevation; a horizontal range

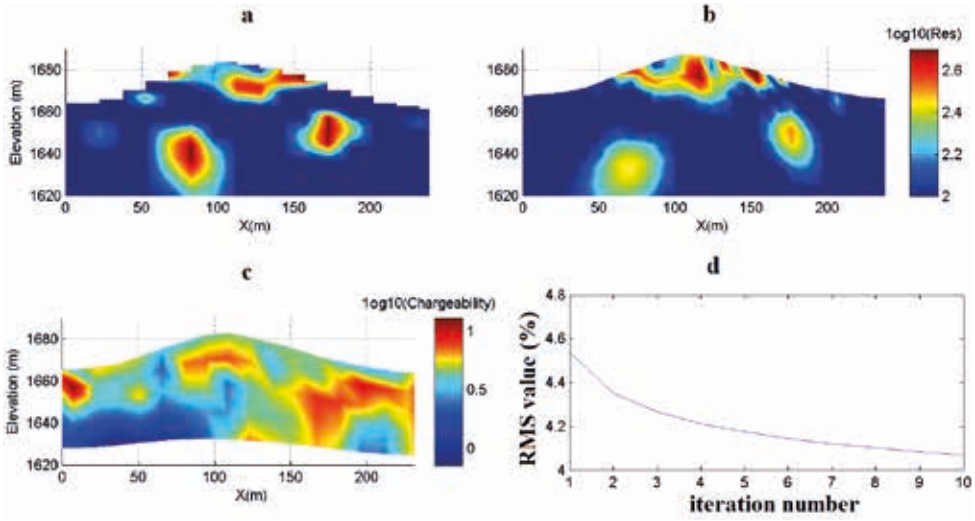

Fig. 7 - Inversion model of DC resistivity data in Iran derived by: a) IE inversion algorithm; b) Res2dinv model; c) Inversion result of IP data obtained from Res2dinv software; d) data misfit RMS errors curve.

of anomaly 3 is approximately from 75 to 120 m with a vertical extension of [1635, 1647 m]. According to our test for compact sources, the depth weighting exponent is equal to 2, while the regularisation parameter and number of iterations are 0.1 and 10, respectively.

According to the inversion results shown in Fig. 7, it can be said that the resistive bodies 1 and 2 inverted by both DC resistivity algorithms agree fairly well with each other and also correspond to IP sources, so that the presence of malachite can be expected. However, the resistive source 3 recovered from inversion by either IE or Res2dinv algorithms cannot be interpreted as malachite because of high resistivity and low chargeability. The RMS of the data misfit, as a goodness-of-fit criterion during the inversion process, for the field example using the IEDW based method is shown in Fig. 7d.

5. Conclusions

Linear IE modelling of DC resistivity is utilised as the basis of this research. The IE inversion modelling of DC resistivity method is extended to the data cases with uneven topography. A damped weighted minimum length solution is adopted for the inversion procedure. Depth weighting is used as the model weighting function and we showed that 2 is the most optimal value for its exponent in the case of compact bodies. Since the forward operator is calculated once during the iterative inversion process, the presented method is very fast and in the investigated cases 20 iterations or less are enough to lead to the desired solutions. The expanded IE inversion algorithm is applied to the synthetic data of a conductive dyke under a valley and resulted in the satisfactory reconstruction of the dyke model. In addition, it retrieved the boundaries of the dyke with more accuracy compared to the Res2dinv inversion model. To conclude, the extended IE inversion for uneven topography was applied to the Robat Sang mine data to evaluate its performance in practical applications. The obtained inverse section showed a high correlation with the inversion model of Res2dinv software.

Data availability. Real data are available and can be shared.

REFERENCES

Aster R.C., Borchers B. and Thurber C.H.; 2018: *Parameter estimation and inverse problems, 3rd ed*. Elsevier, Amsterdam, The Netherlands, 392 pp.

Barahoei H., Rakhshoni E., Fathabadi K. and Moradpour H.; 2014: *A survey on the fauna of Ichneumonidae (Hymenoptera) of Khorasan-e-Razavi province.* Iranian Journal of Animal Biosystematies, 10, 145-160.

Boulanger O. and Chouteau M.; 2001: *Constraints in 3D gravity inversion*. Geophys. Prospect., 49, 265-280.

Cella F. and Fedi M.; 2012: *Inversion of potential field data using the structural index as weighting function rate decay*. Geophys. Prospect., 60, 313-336.

Charré-Meza A.S., Pérez-Flores M.A. and Gómez-Treviño E.; 2000: *2-D inversion of DC resistivity data from the Cerro Prieto geothermal area, Mexico.* In: Iglesias E. (ed), Proceedings World Geothermal Congress 2000 Kyushu - Tohoku, Japan, May 28 - June 10, 2000, International Geothermal Association, Auckland, N.Z., pp. 1037-1041.

Coggon J.H.; 1971: *Electromagnetic and electrical modelling by the finite element method*. Geophys., 36, 132-155.

Demirci I., Erdoğan E. and Candansayar M.E.; 2012: *Two-dimensional inversion of direct current resistivity data incorporating topography by using finite difference techniques with triangle cells: investigation of Kera fault zone in western Crete*. Geophys., 77, 67-75.

Fikos I., Vargemezis G., Zlotnicki J., Puertollano J.R., Alanis P.B., Pigtain R.C. and Sasai Y.; 2012: *Electrical resistivity tomography study of Taal volcano hydrothermal system, Philippines*. Bull. Volcanol., 74, 1821-1831, doi: 10.1007/s00445-012-0638-5.

Fox R.C., Hohmann G.W., Killpack T.J. and Rijo L.; 1980: *Topographic effects in resistivity and induced-polarization surveys*. Geophys., 45, 75-93.

Günther T., Rücker C. and Spitzer K; 2006: *Three-dimensional modelling and inversion of DC resistivity data incorporating topography – II. Inversion.* Geophys. J. Int., 166, 506-517, doi: 10.1111/j.1365-246X.2006.03011.x.

Holcombe H.T. and Jiracek G.R.; 1984: *Three-dimensional terrain corrections in resistivity surveys*. Geophys., 49, 439-452.

Li Y. and Oldenburg D.W.; 1996: *3-D inversion of magnetic data*. Geophys., 61, 394-408.

Li Y. and Oldenburg D.W.; 1998: *3-D inversion of gravity data*. Geophys., 63, 109-119.

Loke M.H.; 2000: *Topographic modelling in electrical imaging inversion*. In: Extended Abstracts 62nd Conference and Technical Exhibition, EAGE, Glasgow, Scotland, p. D-2.

Loke M.H. and Dahlin T.; 2002: *A comparison of the Gauss-Newton and quasi-Newton methods in resistivity imaging inversion*. J. Appl. Geophys., 49, 149-162.

Loke M.H., Acworth R. and Dahlin T.; 2003: *A comparison of smooth and blocky inversion methods in 2D electrical imaging surveys*. Explor. Geophys., 34, 182-187.

Lu D.B., Zhou Q.Y., Junejo S.A. and Xiao A.L.; 2015: *A systematic study of topography effect of ERT based on 3-D modelling and inversion*. Pure Appl. Geophys., 172, 1531-1546.

Menke W.; 2012: *Geophysical data analysis: discrete inverse theory*. Academic Press, London, UK, 293 pp.

Oppliger G.L.; 1984: *Three-dimensional terrain corrections for mise-a-la-masse and magnetometric resistivity surveys*. Geophys., 49, 1718-1729.

Pain C.C., Herwanger J.V., Worthington M.H. and Oliveira C.R.D.; 2002: *Effective multidimensional resistivity inversion using finite-element techniques*. Geophys. J. Int., 151, 710-728.

Paoletti V., Ialongo S., Florio G., Fedi M. and Cella F.; 2013: *Self-constrained inversion of potential fields*. Geophys. J. Int., 195, 854-869.

Penz S., Chauris H., Donno D. and Mehl C.; 2013: *Resistivity modelling with topography*. Geophys. J. Int., 194, 1486-1497.

Pérez -Flores M.A., 1995: *2-D fast inversion of DC resistivity and MT data of CSEM measurements at low induction numbers.* PhD thesis, CICESE, Baja California, Mexico.

Pérez-Flores M.A., Méndez-Delgado S. and Gómez-Treviño E.; 2001: *Imaging low-frequency and dc electromagnetic fields using a simple linear approximation*. Geophys., 66, 1067-1081, doi.org/10.1190/1.1487054.

Sasaki Y.; 1994: *3D resistivity inversion using the finite-element method*. Geophys., 59, 1839-1848.

Shi-zhe X.; 1993: *The effect of two-dimesional terrain with point source on resistivity surveys*. Geophys. Res. Lett., 20, 891-894.

Shin Y., Shin S., Cho S.J. and Son J.S.; 2021: *Application of 3D electrical resistivity tomography in the Yeoncheon titanomagnetite deposit, South Korea*. Minerals, 11, 563, doi: 10.3390/min11060563.

Spitzer K.; 1995: *A 3-D finite-difference algorithm for DC resistivity modelling using conjugate gradient methods*. Geophys. J. Int., 123, 903-914.

Szűcs P., Szabó N.P., Zubair M. and Szalai S.; 2021: *Innovative hydrogeophysical approaches as aids to assess Hungarian groundwater bodies*. Appl. Sci., 11, 2099, doi: 10.3390/app11052099.

Telford W.M., Geldart L.P. and Sheriff R.E.; 1990: *Applied geophysics*. Cambridge University Press, Cambridge, UK, 770 pp.

Tikhonov A.N. and Arsenin V.I.; 1977: *Solutions of ill-posed problems.* SIAM Review, 21, 266–267.

Tong L.T. and Yang C.H.; 1990: *Incorporation of topography into two-dimensional resistivity inversion*. Geophys., 55, 354-361.

Tsokas G.N., Tsourlos P.I., Vargemezis G. and Novack M.; 2008: *Non-destructive electrical resistivity tomography for indoor investigation: the case of Kapnikarea church in Athens*. Archaeolog. Prospect., 15, 47-61, doi. org/10.1002/arp.321.

Tsourlos P.I., Szymanski J.E. and Dittmer J.K.; 1995: *The topographic effect in earth resistivity arrays: a comparative study*. In: Proc. 1995 International Geoscience and Remote Sensing Symposium, IGARSS'95, Quantitative Remote Sensing for Science and Applications, Firenze, Italy, Vol. 1, pp. 30-32, doi: 10.1109/IGARSS.1995.519639.

Tsourlos P.I., Szymanski J.E. and Tsokas G.N.; 1999: *The effect of terrain topography on commonly used resistivity arrays*. Geophys., 64, 1357-1363.

Varfinezhad R. and Ardestani V.E.; 2022: *Kernel based regularization parameter and source dependent depth weighting in gravity inversion*. Bull. Geoph. Ocean., 18 pp., doi: 10.4430/bgo00372.

Varfinezhad R., Parnow S. and Kamkar Rouhani A.; 2019: *2-D inversion of magnetic data using compactness and depth weighting constraints: two case studies on gas transmission pipe and archeological data.* J. Earth Space Phys., 45, 507-521.

Varfinezhad R., Oskooi B. and Fedi M.; 2020: *Joint inversion of DC resistivity and magnetic data, constrained by cross gradients, compactness and depth weighting*. Pure Appl. Geophys., 177, 4325-4343, doi: 10.1007/s00024-020-02457-5.

Corresponding author: Ramin Varfinezhad
nstitute of Geophysics, University of Tehran
Northern Kargar, Tehran, Iran
Phone: +98 919 8203127; e-mail: ramin.varfi@ut.ac.ir

Appendix A

First, the inversion results of the IE method (for $\beta = 1$) are compared with Res2dinv software. We then discuss why the regularisation parameter is equal or close to the maximum value of forward operator results in a desired model.

Four conductive anomalies (other arrays)

This section extends our study to other geo-electrical arrays, again using the model consisting of four conductive bodies. Fig. A1 shows the reconstructed models from the IE inversion method and the Res2dinv algorithm.

Pole-dipole. The source reconstructed by the IE and Res2dinv algorithms are relatively similar, except the second source, which is retrieved better by the IE inversion algorithm; in fact, such source shows too large a depth extent in the Res2dinv section.

Pole-pole. We obtain a similar result: the second source is not well recognised by the Res2dinv algorithm and extends deeply. Res2dinv algorithm cannot recover the third source whose depth to top (10 m) is twice its size (5 m in *x* and *z* directions).

Wenner-Alfa. The Res2dinv algorithm defines the third source poorly, the tabular source is too deeply elongated and the second source is not well-resolved at large depths. For the first two

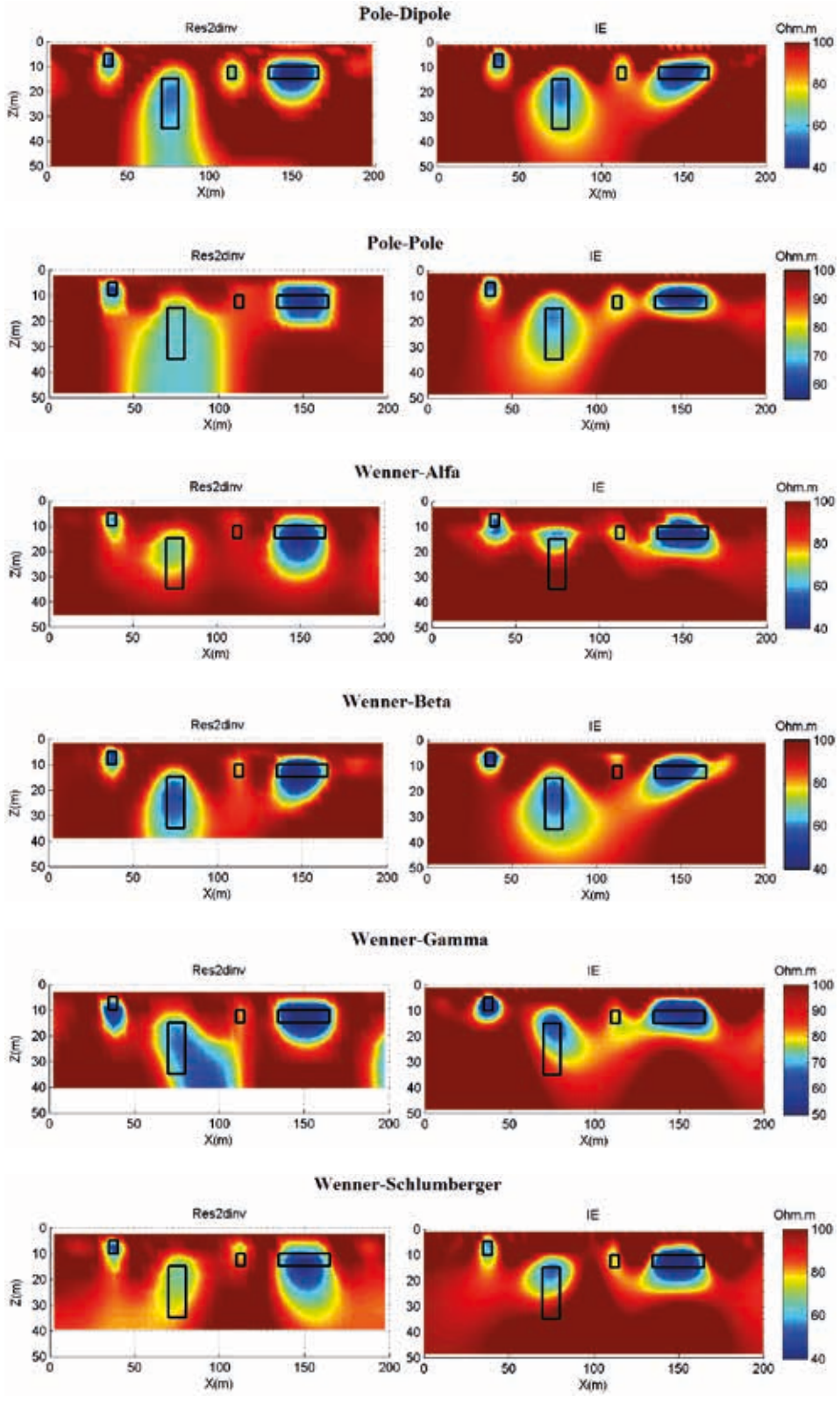

Fig. A1 - Inversion results derived from the synthetic data of four conductive models for different geo-electrical arrays.

bodies the IE algorithm yields similar results, while for the other two sources it allows a better definition.

Wenner-Beta. Both methods retrieve approximately the same source models, but the rightmost source derived by the IE algorithm matches the true position better.

Wenner-Gamma. For this array, we see that the IE algorithm better defines all the four sources and the Res2dinv algorithm also presents some false source reconstructions at the borders.

Wenner-Schlumberger. On the whole, the IE algorithm yields a better inversion model. The Res2dinv method generates a false model between the first two sources.

We have therefore found that our algorithm yields a fairly correct source reconstruction for this multisource model, no matter the kind of array used. Regularisation parameter, depth weighting exponent, and number of iterations, the three involved parameters in the inversion procedure of the IE algorithm, are described in Table A1.

According to Table A1, we conclude that:

I) the regularisation parameter value used in the inversion process is usually close to the maximum value of the kernel matrix **A**;

II) in general, $\beta = 1$ is a good choice for the depth weighting exponent. Ten iterations are enough to get good results.

Table A1 - The maximum value of the forward operator, regularisation parameter, exponent of depth weighting, number of iterations, and RMS misfit errors for the IE inversion algorithm results.

	Dipole-dipole	Pole-dipole	Pole-pole	Wenner Alfa	Wenner Beta	Wenner Gamma	Wenner Schlumberger
Maximum of A	0.17	0.22	0.08	0.19	0.18	0.11	0.2
μ	0.2	0.2	0.06	0.20	0.18	0.1	0.15
β	1	1	1	1	1	1	1
Number of iterations	10	10	10	10	10	10	10
RMS error (%)	2.05	1.85	0.84	1.70	1.70	1.62	0.76

Why does a regularisation parameter equal or close to the maximum value of the forward operator lead to a desirable solution?

To explain this, we focus on the term of $(\mathbf{W}_m^{-1}\mathbf{A}^T)\,(\mathbf{A}\mathbf{W}_m^{-1}\mathbf{A}^T + \mu\mathbf{W}_d)^{-1}$ from Eq. 11, which can be rewritten as $[(\mathbf{A}\mathbf{W}_m^{-1}\mathbf{A}^T + \mu\mathbf{W}_d)\,(\mathbf{W}_m^{-1}\mathbf{A}^T)^{-1}]^{-1}$ and compute the singular value decomposition (SVD) of $\boldsymbol{S} = (\mathbf{A}\mathbf{W}_m^{-1}\mathbf{A}^T + \mu\mathbf{W}_d)\,(\mathbf{W}_m^{-1}\mathbf{A}^T)^{-1}$ in four cases:

a) $\mu = 0$;

b) $\mu = 0.1 \times \max(\mathbf{A})$;

c) $\mu = \max(\mathbf{A})$;

d) $\mu = 10 \times \max(\mathbf{A})$.

The case of the dipole-dipole array is illustrated. Fig. A2 represents the images of the singular values corresponding to the four mentioned cases. It can be observed that when $\mu = 0$, there are many singular values close to zero (here, singular values after 30 are very close to zero). Therefore, truncated singular value decomposition (TSVD) is required to solve the instability of the solution and here we should make the cut off at about the 30th singular value. By considering $\mu = 0.1 \times \max(\mathbf{A})$ the situation changes and TSVD is necessary by cutting of at about the 75th singular value, because allowing more singular values to be included in the inversion procedure

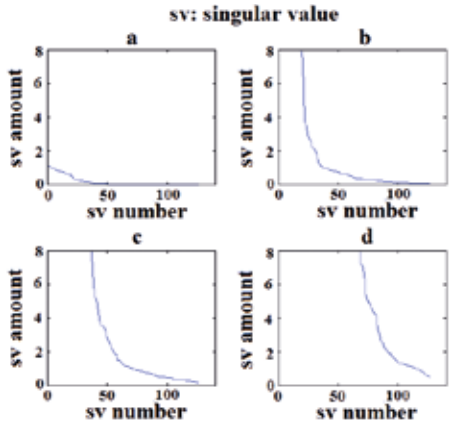

Fig. A2 - Plots of the singular value (diagonal elements) for the cases of: a) μ = 0; b) μ = 0.1 x max(**A**); c) μ = 1 x max(**A**); and d) μ = 10 x max(**A**).

leads to an unstable solution and in the presence of noise this situation can worsen. For the case μ = max(**A**), it can be observed that singular values follow a reducing trend, but they are not equal to zero. Therefore, instability of the solution is solved and since the singular values are small, the introduced bias in the solution is not significant. In other words, small singular values give small levels of contribution to the model solution; hence, the model resolution is also satisfied. In the last case, μ = 10 × max(**A**) leads to a really stable solution, but the resolution of the inverse solution decreases substantially because of the large coefficients (singular values) multiplied by eigenvectors making up the model.

Appendix B

Loke *et al.* (2003) defined a versatile algorithm to solve the resistivity problem used in the widespread Res2dinv® software. It is the l_2 norm smoothness-constrained optimisation (SCO) method producing a model with a smooth variation of resistivity values. In this case, at each k^{th} iteration, the following objective function is minimised:

$$\Psi(\mathbf{m_k}) = \mathbf{g}_k^T\mathbf{g}_k + \mu_k\mathbf{m}_k^T\mathbf{W}_m\mathbf{m}_k \quad \text{(B1)}$$

which is acquired by presuming independent measurements with unit variance so that $\mathbf{W_d} = \mathbf{I}$, $\mathbf{W_m} = \alpha_x\mathbf{C_x^TC_x} + \alpha_z\mathbf{C_z^TC_z}$, where $\mathbf{C_x}$ and $\mathbf{C_z}$ are smoothness matrices in x and z directions, respectively, and α_x, and α_z are the relative weights. For the k^{th} iteration, μ_k and $\mathbf{m}_k$ are the damping factor and the model parameters vector, respectively, and $\mathbf{g}_k = \mathbf{d} - \mathbf{F}(\mathbf{m})$ is the data misfit vector containing the difference between the measured and computed data. Taking into consideration the gradient of the objective function, the Gauss-Newton least-squares results in solving the following system of equations (e.g. Loke and Dahlin, 2002):

$$\left(\mathbf{J}_k^T\mathbf{J}_k + \mu_k\mathbf{W}_m\right)\Delta\mathbf{m}_k = \mathbf{J}_k^T\mathbf{g}_k - \mu_k\mathbf{W}_m\mathbf{m}_{k-1} \quad \text{(B2)}$$

$\mathbf{J}_k$ is the Jacobian matrix. Obtaining $\Delta\mathbf{m}_k$ (the model variation), the inversion model is updated as $\mathbf{m}_k = \mathbf{m}_{k-1} + \Delta\mathbf{m}_k$.